Hover Performance of a Cycloidal Rotor for a Micro Air Vehicle



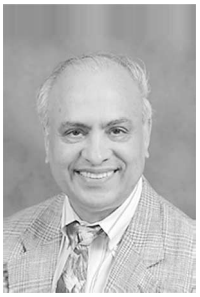

Jayant Sirohi* — *Assistant Research Scientist*
Eric Parsons — *Graduate Research Assistant*
Inderjit Chopra — *Alfred Gessow Professor and Director*
Alfred Gessow Rotorcraft Center, Department of Aerospace Engineering, University of Maryland, College Park, MD

In recent years, interest has been growing in a new class of very small flight vehicles called micro air vehicles (MAVs). Hover capability is highly desirable with respect to the mission requirements of these vehicles. Due to the small size of MAVs and the low Reynolds number regime in which they operate, scaling down conventional rotorcraft configurations to the MAV scale may not yield optimum performance. Unconventional vehicle configurations can be explored to realize high endurance hover capable MAVs. This paper investigates the hover performance of a small-scale cycloidal rotor to determine its viability for use in a micro air vehicle. A 6 inch diameter prototype rotor was constructed and tested to determine the effects of number of blades, blade pitch angle, and rotational speed on thrust output and power requirements. Pressure distribution was measured to obtain insight into the downwash and flow through the rotor. An analytical model, using a combination of vertical axis wind turbine theory and an indicial solution for the aerodynamic response was developed to predict rotor performance, and was validated with the experiments. The performance of the cycloidal rotor was compared to that of a conventional rotor of the same diameter in terms of power loading. Based on the analytical model and the experimental results, a conceptual design of an MAV utilizing cycloidal propulsion was developed. The conceptual cyclo-MAV utilizes two cycloidal rotors, providing thrust, propulsion, and control. Complete vehicle weight is envisaged to be 240 g, with two three-bladed rotors of six inches diameter.

Nomenclature

AR	aspect ratio of blade
a	location of pivot point of the airfoil measured from mid-chord, aft positive
b	semi-chord of airfoil
b_r	span of the cycloidal rotor
C_L^c	circulatory lift coefficient of blade
$C_{L_\alpha}^c$	circulatory lift curve slope of blade
c	airfoil chord
d	rotor diameter
dA	elemental area of actuator disk used in momentum analysis
dT	thrust of actuator disk element
e	Oswald span efficiency factor
F_{norm}	force produced by a blade normal to its circular path around the rotor azimuth
F_{res}	resultant force of F_x and F_z
F_{tan}	force produced by a blade tangential to its circular path around the rotor azimuth
F_x	force produced by a blade in the horizontal (x) direction
F_z	force produced by a blade in the vertical (z) direction
k	reduced frequency
l	total lift of the airfoil
l^c	circulatory lift of the airfoil
M_a	aerodynamic moment about the pitching axis of the airfoil
M_{tot}	total moment about the pitching axis of the airfoil
$\dot{m}$	mass flow rate
N_b	number of blades
P	power required by the rotor
Q	rotor torque
R	rotor radius
Re	Reynolds number
v_d	induced velocity, downstream half of rotor
v_u	induced velocity, upstream half of rotor
V_∞	far upstream velocity of upstream half of rotor
w	far wake induced velocity of upstream half of rotor and far upstream velocity of downstream half of rotor
w_∞	far wake induced velocity of downstream half of rotor
α	angle of attack
α_{dw}	induced angle of attack
δ	Dirac function
θ	blade pitch angle measured with respect to the tangent of the blade's circular path around the rotor azimuth
θ_{max}	amplitude of the blade pitch oscillation
ϕ	phase angle of eccentricity of the rotor measured counterclockwise from the negative z axis
ϕ_s	Wagner's function
Ψ	blade position around the azimuth of the rotor measured counterclockwise from the negative z axis
Ω	rotational speed of cycloidal rotor
ω	angular velocity of blade about pivot point

Introduction

Recent interest in micro air vehicles (MAVs) has developed, in part, due to the changing needs of the military as the battlegrounds of the

*Corresponding author; email: sirohij@umd.edu.

Manuscript received May 2006; accepted March 2007.

future move to restricted, highly populated urban environments where conventional aircraft lose much of their utility. Hover capability is highly desirable in these environments for missions such as surveillance. Several hovering MAVs based on scaled down single main rotor and coaxial helicopter configurations have been successfully built and flight tested (Refs. 1, 2). These MAV scale rotors typically operate in the Reynolds number range from 10,000 to 100,000. Consequently, they experience much higher viscous drag than conventional helicopter rotors. As a result, MAV scale rotors suffer from an inherent limitation in aerodynamic efficiency, which translates into poor endurance (Ref. 3). By careful design of rotor blade geometric parameters such as solidity, twist, taper, camber, and tip shape (Refs. 2, 4) the maximum figure of merit achieved to date for a rotor of diameter 9 inches is around 0.64, and for a rotor of diameter 6 inches is around 0.55 (Ref. 5), at a tip Reynolds number of 40,000. In comparision, a conventional helicopter rotor with a figure of merit of 0.64 is considered poor in terms of aerodynamic efficiency. In fact, most of the modern helicopter rotors have a figure of merit of about 0.75–0.8 (Ref. 6).

An MAV based on a cycloidal rotor is proposed as an alternative to helicopter based MAVs. The concept of cycloidal propulsion is quite old, but it has remained relatively obscure until recently. Kirsten (Ref. 7) investigated cycloidal propulsion at the University of Washington in the 1920s. He constructed a large cycloidal propeller and investigated its use in air vehicles. However, he subsequently began to explore applications of the cycloidal rotor in marine systems, and today, these are used extensively in tug boats, to provide them with the maneuverability necessary to operate in confined harbors. In the 1930s, Wheatley (Refs. 8, 9) developed a simplified aerodynamic theory of a cyclogiro rotating wing and conducted wind tunnel tests on a large four-bladed prototype rotor with diameter and span of 8 feet. The blades incorporated a NACA 0012 airfoil profile and had a chord of 0.312 ft. Significant thrust levels were measured but poor agreement between theory and experiment was achieved mainly due to incomplete knowledge of forces on oscillating airfoils. Cycloidal rotors have also been proposed for use on airships (Refs. 10, 11) as they can result in significantly increased maneuverability.

More recently, Gibbens et al. (Ref. 12) proposed a UAV configuration with a gross weight of 600 lb, having two cycloidal rotors to produce lift and propulsion. A full scale experimental setup was constructed to measure the thrust produced and power consumed by a single cycloidal rotor. The rotor had a span of 4 ft, a diameter of 4 ft and six blades of chord 1 ft with a NACA 0012 airfoil. A maximum power loading of 10.88 lb/HP was recorded, and the rotor operated at a maximum Reynolds number of around 730,000. A significant lack of noise was observed during operation. McNabb (Ref. 13) developed a computer model for this cycloidal rotor and compared the predictions with experimental results.

Kim et al. (Ref. 14) experimentally investigated the performance of a cycloidal rotor with a span of 0.8 m. The blades used a NACA 0012 airfoil, with a chord of 0.15 m. Rotor thrust and torque were measured, and the effect of blade pitch angle, rotor radius, and number of blades were studied up to a rotational speed of 600 rpm, corresponding to a Reynolds number of around 260,000. It was observed that thrust was proportional to the square of rotational speed, and power was proportional to the cube of rotational speed. A maximum power loading of around 12 kgf/HP was observed at low thrust levels, which asymptotes to around 5 kgf/HP at high thrust. An analysis was also conducted using commercial CFD software to predict rotor characteristics. Yun et al. (Ref. 15) designed a VTOL UAV with cycloidal rotors intended to have a take-off weight of 50 kg. Hwang et al. (Ref. 16) optimized the aerodynamic and structural design of a VTOL UAV using four cycloidal rotors of radius 0.85 m, as well as designed a micro-scale cyclocopter with two cycloidal rotors of radius 0.2 m.

Vertical axis windmills (VAWTs) experience a motion similar to cycloidal rotors although they generally possess fixed pitch blades. A large body of work has been conducted in developing aerodynamic performance prediction methods for these windmills (Refs. 17–19). In addition, a small percentage of VAWT designs incorporate variable blade pitch similar to the cycloidal blade system.

The cycloidal blade system may be considered as a horizontal rotary wing, with its blade span parallel to a horizontal axis of rotation. As the blades rotate around the azimuth, their pitch angle is varied periodically. Each spanwise blade element operates at about the same conditions—velocity, Reynolds number, angle of attack, centrifugal force—and thus can be designed to operate at its optimum efficiency. Due to the highly unsteady flow field and the constant angle of attack over the entire span of the blade, a cycloidal rotor may exhibit better performance than a conventional rotor at the MAV scale. Figure 1 shows the approximate power loading of several production helicopters as well as a few experimental cycloidal rotors. It can be seen that in general, cycloidal rotors exhibit a higher power loading than conventional helicopters. This improved power loading is very attractive for exploring cycloidal propulsion on the MAV scale. In addition, a cycloidal rotor has the ability to change the direction of thrust almost instantly, resulting in good maneuverability at low freestream velocities, which is highly desirable for MAV operation in confined areas.

Although existing literature seems to show that the cycloidal rotor is superior to a conventional rotor in terms of power loading, it is unclear how they compare with respect to a constant linear dimension. This information is critical to the choice of a configuration for an MAV. In addition, other metrics such as hover figure of merit must be investigated, with which a meaningful comparison can be made. The studies described above involved testing of large-scale models, at relatively high Reynolds numbers. It remains uncertain how the design would translate to an MAV-scale vehicle, operating at a maximum Reynolds number of less than 20,000. None of the previous studies had a comprehensive analysis that matched well with their experimental results and could be used as a preliminary design tool. The present research aims to address some of these issues.

The primary objective of the present research was to determine whether a cycloidal rotor configuration is a viable means of propulsion for an MAV. A secondary objective was to develop a simple analytical tool for predicting the performance of a cycloidal rotor and to validate the analysis with experiments. These objectives are carried out by characterizing the performance of a small-scale cycloidal rotor of diameter and span of 6 inches. Performance of the rotor was studied by determining thrust and torque of the rotor as a function of number of blades, blade pitch angle and rotational speed. A theoretical model was developed incorporating unsteady aerodynamic effects, and was validated with experiments. An investigation of the flow field around the model rotor was conducted by measuring the pressure distribution below the rotor and across its cross-section. The efficiency of the cycloidal rotor was compared with that of a conventional rotor of the same diameter, both in terms of power loading and figure of merit. Finally, the analysis was used to perform a preliminary design of an MAV utilizing cycloidal propulsion. Weights and constraints were applied using CAD software to determine if the rotors could provide the necessary thrust and if the construction of the vehicle on the MAV scale was feasible.

Operating Principle

A cycloidal rotor consists of several blades that rotate about a horizontal axis that is perpendicular to the direction of flight (Fig. 2). Blade span is parallel to the axis of rotation. The pitch angle of each of the blades is varied such that it changes periodically about the

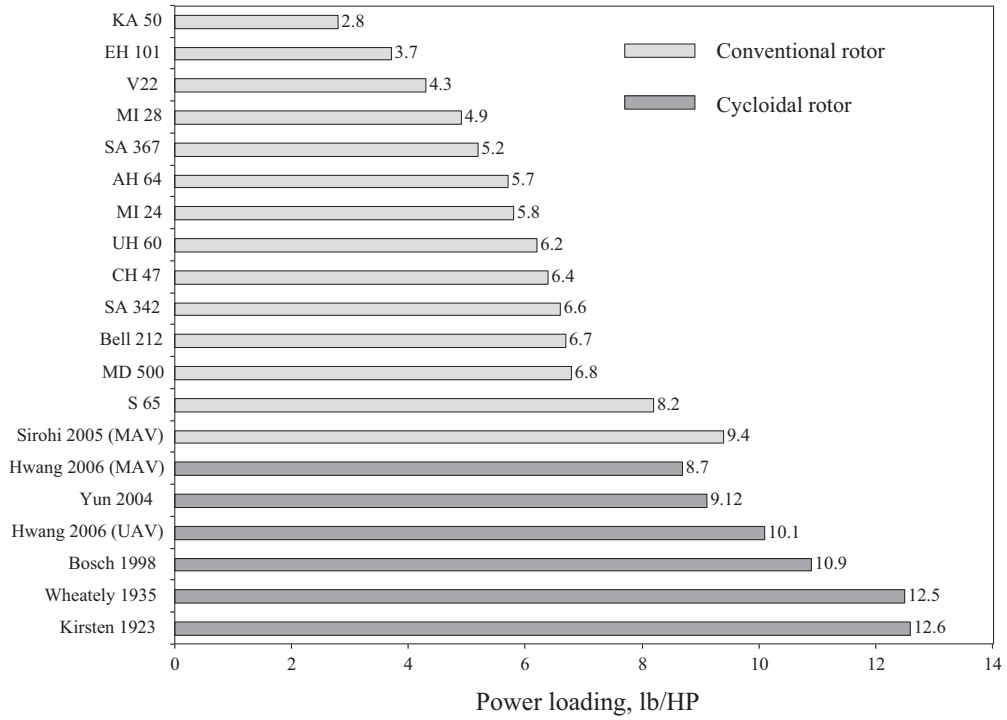

Fig. 1. Comparison of power loading of conventional rotors and cycloidal rotors (adapted from Ref. 12).

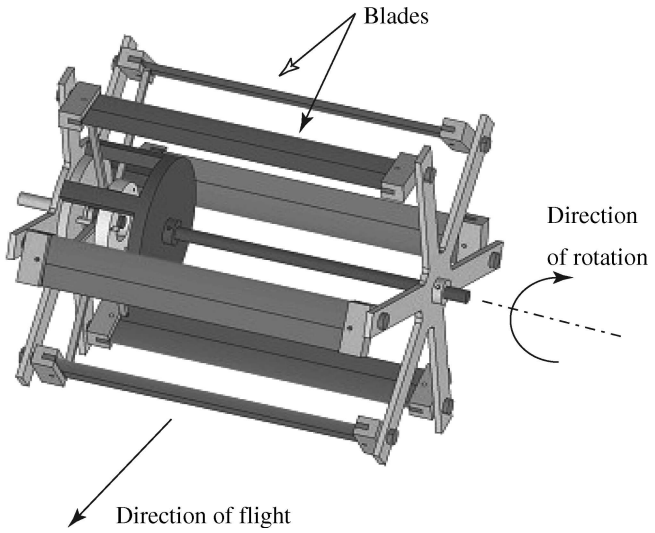

Fig. 2. Cycloidal rotor configuration.

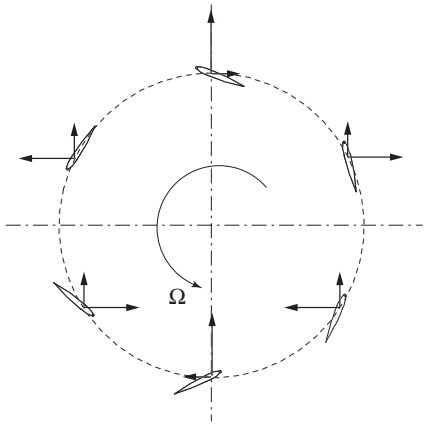

Fig. 3. Thrust vectors at each blade cross-section.

airfoil quarter-chord as the blade moves around the azimuth of the rotor.

Each of the blades produces a lift and a drag force. Blades at the top and bottom positions produce an almost vertical net force, while those at the sides produce small lateral forces because of their reduced angle of attack. Figure 3 shows a cross-section of a six-bladed cycloidal rotor rotating with an angular velocity Ω. The horizontal and vertical components of the force acting on each blade is also shown. It can be seen that the sum of the horizontal components is zero, resulting in a net vertical thrust. In addition, the amplitude and phase of the maximum blade pitch angle may be changed, resulting in a change of the magnitude and direction of the net thrust vector of the rotor.

Experimental Setup

Experiments were performed on a prototype cycloidal rotor to obtain an understanding of the flow field around the rotor as well as to carefully measure the performance of the rotor in terms of thrust produced and power consumed. Two separate experimental setups were constructed. The first setup was dedicated to investigating the flow field by measuring the pressure distribution in the downwash and along the cross-section of the rotor. The second setup consisted of a fixture with load cells to measure the rotor thrust, torque and rotational speed.

Prototype cycloidal rotor

A prototype cycloidal rotor was constructed with six blades and a diameter and blade span of six inches. The blades use a NACA 0010 airfoil profile and have a one inch chord. The rotor could also be tested in

Table 1. Geometry of linkages used on experimental rotor

Linkage	Length (inch)
L_1	2.331
L_2	0.180 (variable)
L_3	2.369
L_4	0.426

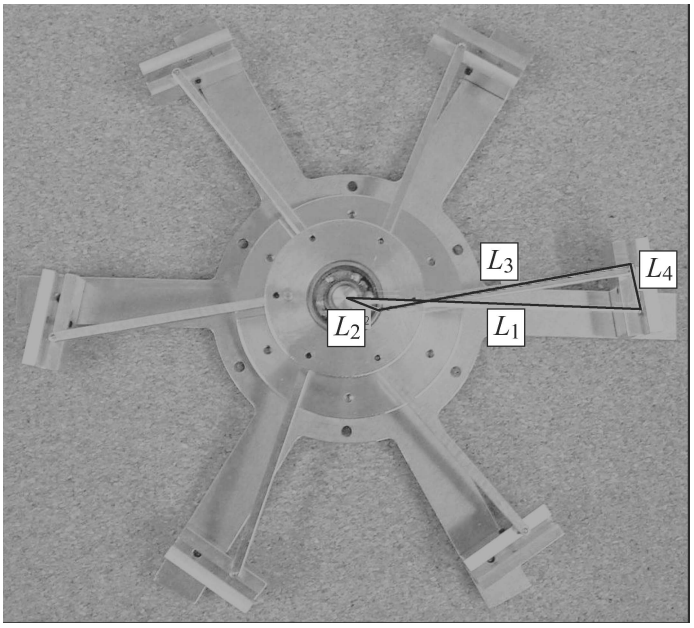

Fig. 4. Offset mechanism four bar linkage.

a three-bladed configuration. The main structural elements of the design consists of two end plates, to which each of the blades is attached. The two end plates are also connected to each other by a rigid shaft, and the assembly rotates around another concentric shaft.

The required blade pitch motion around the rotor is achieved by a passive mechanism and the only power required for its operation is to overcome both the friction associated with its moving components and the inertial forces associated with the oscillatory change in pitch. The mechanism consists of both fixed and rotating parts. A shaft is offset from the center of rotation of the rotor. This offset piece is fixed, and its orientation sets the direction of the thrust vector for the rotor. Attached to this offset piece is a bearing and a rotating disk, to which six linkages are attached. Each of the linkages connects to the trailing edge of one of the blades. Together, the system comprises a crank-rocker type four bar linkage, which is used to accomplish the required change in blade pitch angle (Fig. 4). The offset piece was designed so that the blade pitch angle amplitude could be set from 0° to 40° by changing the linkage length L_2. Note that the blade pitch angle is defined at any azimuth as the angle between the mean chord line of the airfoil and the tangent to the circular path of the airfoil at that azimuth. Another important geometric parameter is the eccentricity ϕ, which defines the azimuthal location of the maximum blade pitch angle. Table 1 provides the lengths of the linkages.

The blades for the cycloidal rotor are constructed of carbon fiber composite wrapped around a foam core. Note that because of the constraint that they must operate effectively at both positive and negative angles of attack, the symmetric NACA 0010 profile was used for the airfoils. The

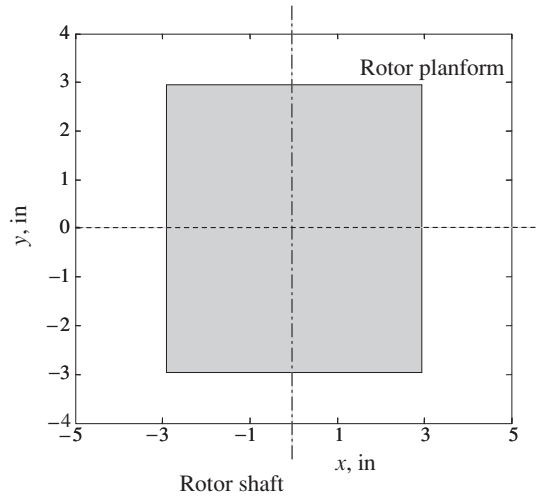

Fig. 5. Definition of the coordinate axes for pressure measurement, below the rotor.

rotor was driven by a brushless motor, and all components were weighed and balanced within 0.01 g.

Measurement of flow field around the rotor

Experiments were performed to investigate the flow field around the cycloidal rotor by means of total pressure measurements, in order to obtain a physical feel of the downwash distribution and thrust production mechanism. As some uncertainity exists in the exact flow direction, a 1/16 inch diameter Kiel probe was used to measure the total pressure, because such a probe is insensitive to entry cone angles of up to 45°. The goal of these experiments was to obtain a qualitative picture of the flow field around the rotor, as well as to measure the velocities in the downwash of the rotor. The prototype cycloidal rotor was supported in two different configurations for this testing. In the first case, the cycloidal rotor was supported on one end only, in a cantilevered condition. In the second case, both ends of the rotor were supported and the rotor was effectively in a clamped–clamped condition. In both cases, the axis of rotation of the cycloidal rotor was horizontal.

A differential pressure transducer (0–50 Pa range) was used to record the pressure. Pressure measurements were recorded at one-inch increments in both the x and y directions (in the horizontal plane). The measurements were then repeated at locations of 0.5, 3, 6, and 9 inches below the rotor (vertical plane). Rotational speed was kept constant at 1100 rpm. Vertical movement was achieved by mounting the probes on a height gauge, with a precision of ± 0.001 inch. Movement in the x and y directions was accomplished by mounting the height gauge to a two degree-of-freedom x–y positioning stage driven by stepper motors that allowed for movements with a precision of ± 0.001 inch. The coordinate axes used in the measurement of the downwash distribution are defined in Fig. 5. Measurements were recorded from $x = -5$ inch to $x = 5$ inch and $y = -4$ inch to $y = 4$ inch.

Measurements were also taken along the rotor flow cross-section for the rotor in the clamped condition. The Kiel probe was located at the center of the blade span, and pressure measurements were recorded in the x and z directions in one-inch increments from $x = -5$ inch to $x = 5$ inch and $z = -4$ inch to $z = 4$ inch. Figures 5 and 6 define the coordinate axes for this testing. Note that due to the geometry of the setup, these measurements could be performed only outside the rotor.

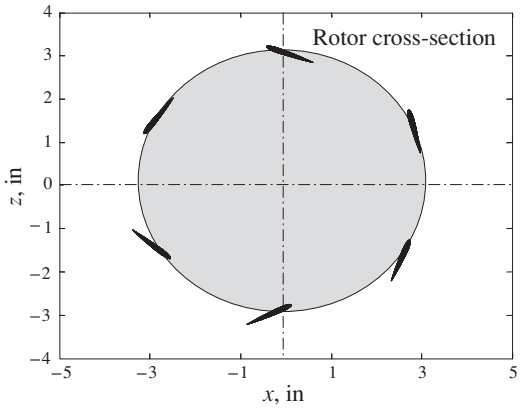

Fig. 6. Definition of the coordinate axes for pressure measurement, cross-section of the rotor.

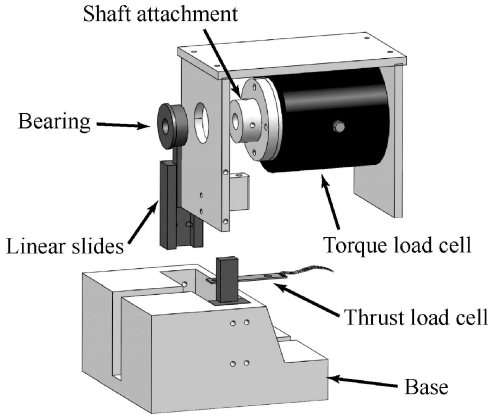

Fig. 8. Torque measurement in the cycloidal rotor test stand.

Measurement of loads and power

A test rig was constructed to measure mechanical as well as electrical power consumed by the cycloidal rotor. Figures 7 and 8 illustrate the construction of the test rig. The rotor is mounted on a nonrotating shaft, which runs through bearings mounted in vertical plates at each end. Each vertical plate is mounted on a linear slide, preventing horizontal motion and minimizing friction. Each plate is attached to a load cell, which is, in turn, attached to the base. As a result, the load cells measure the vertical force at each end of the nonrotating shaft. The sum of these forces gives the total thrust produced by the rotor.

The drive motor is mounted on the nonrotating shaft and is connected to the rotor by a spur gear. One end of the nonrotating shaft is attached to a torque load cell, which is clamped to one of the vertical plates. Therefore, as the drive motor is not clamped to the base, the torque load cell measures the total torque on the rotor system. The rotational speed of the rotor is measured by a Hall sensor.

A range of tests were performed to characterize the performance of the rotor. Measurements were taken at blade pitch angle amplitudes of 10, 20, 30, and 40° for rotational speeds ranging from 0 to 1200 rpm. The tests, were conducted with six blades and were repeated with three blades to determine the effect of the number of blades on the performance of the rotor. A series of tests were also performed to determine the effect of blade pitch angle on the direction of the resultant thrust vector. Measurements were recorded for blade pitch angles ranging from 0 to 40° and eccentricity, ϕ, varying from $-50°$ to 50°. Rotational speed was held constant at 800 rpm for these tests. To determine the power required by the rotor to overcome mechanical friction, tare tests were performed with all blades removed. These tare tests were conducted for blade pitch angles from 0 to 40°, with rotational speeds ranging from 0 to 1200 rpm. The aerodynamic power consumed was calculated by subtracting the tare (mechanical) power from the total power.

Analytical Procedure

An analytical model of a cycloidal rotor was developed to predict the magnitude and direction of thrust as well as power requirements of a cycloidal rotor in hover. The goal is to develop a simple model of cycloidal rotor performance, based on existing momentum theory analysis of vertical axis wind turbines, for use as a design tool. To calculate the performance of the rotor, the azimuthal position and pitch angle of each blade must be determined. This can be calculated from the kinematics of the four bar mechanism used to create the pitch change. From the pitch angle of each blade and the rotor downwash, the angle of attack of each blade can be determined. Lift and drag forces are calculated based on unsteady aerodynamics. The forces from each blade are summed to find the total vertical and horizontal forces for the rotor. Downwash is determined

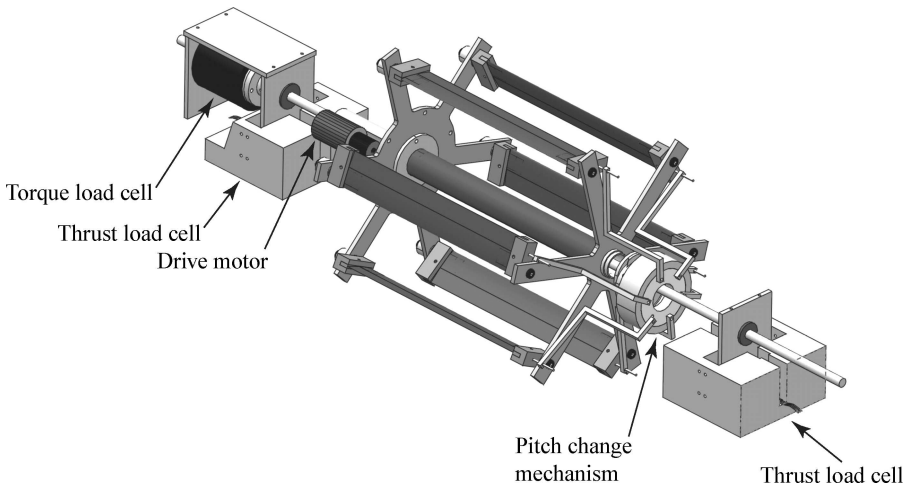

Fig. 7. Cycloidal rotor test setup.

from the resultant thrust using a modified version of momentum theory and is used to calculate the induced angle of attack. An iterative procedure is then executed until convergence is achieved for lift and drag forces. The rotor is then rotated by an incremental amount and the process is repeated to calculate the rotor forces as a function of azimuth.

Coordinate system

Figure 9 shows the coordinate system used for the analysis. The azimuthal position of the blade, Ψ, is measured counterclockwise from the negative z-axis. From Fig. 10, ϕ is the phase angle of eccentricity, used to define the direction of thrust, and is measured counterclockwise from the negative z-axis. Blade pitch angle (θ) is measured with respect to the tangent of the blade's circular path. Velocities and forces are positive upward as well as in the direction of rotation and radially outward.

The coordinate system for the airfoil is shown in Fig. 11. The airfoil is represented as a line extending from the leading edge at chordwise location $x = -1$ to the trailing edge at $x = +1$. The axis of rotation, or pitching axis, for the airfoil is located at point a. The airfoil may experience movement in the vertical direction, h, measured positive downward, or rotation about $x = a$, positive in the nose-up direction. The incident velocity v moves from left to right. The angle of attack α is defined as the angle between the velocity v and the instantaneous position of the airfoil chord line.

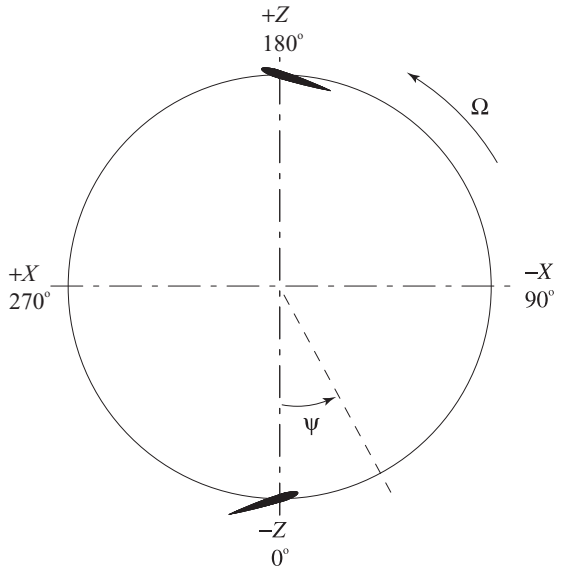

Fig. 9. Definition of coordinate system for analysis.

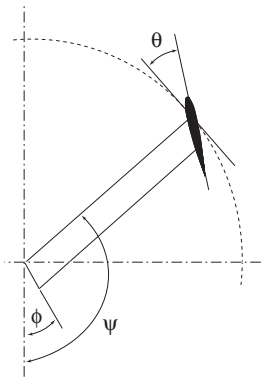

Fig. 10. Pitch angle definition for the cycloidal rotor.

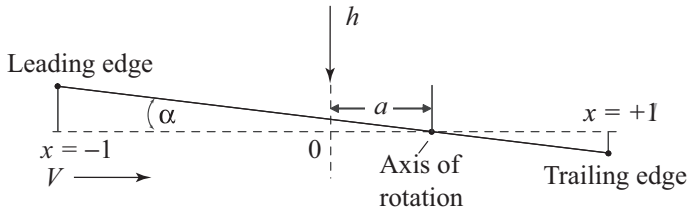

Fig. 11. Airfoil coordinate system.

Unsteady aerodynamics

Each rotor blade experiences a highly unsteady aerodynamic environment as it rotates around the azimuth. This includes the periodic oscillation in angle of attack due to the pitch change mechanism, the effects of the previous blade wake, three-dimensional effects, and dynamic stall at high angles of attack. Reduced frequency is defined as

$$k = \frac{\omega b}{V} \tag{1}$$

where b is the airfoil semi-chord, ω is the frequency of oscillation and V is the incident velocity. The reduced frequency of the cycloidal rotor is given by

$$k = \frac{\omega c}{2V} = \frac{c}{2R} \tag{2}$$

Note from Eq. (2) that the reduced frequency simplifies to a geometric ratio independent of rotational speed and as such, its meaning is ambiguous. Substituting values for the chord and radius of the present cycloidal rotor prototype results in a reduced frequency of $k = 0.167$. Typically, for $k > 0.2$, the flow is highly unsteady, and unsteady effects will begin to dominate the behavior of the airloads (Ref. 20). Therefore, unsteady effects are included in the present analysis.

The methodology used to arrive at the forces in the present analysis relies on a time domain formulation. Wagner's function is used to solve for the indicial lift on an airfoil undergoing an incremental change in angle of attack. Note that the application of Wagner's function to the present problem is an approximation, as the wake from the trailing edge of the airfoil is not planar. However, this assumption is considered acceptable for the present analysis.

The variation in lift coefficient for a step change in angle of attack as given in Ref. 20 is

$$C_l(t) = \frac{\pi c}{2V}\delta(t) + 2\pi\alpha\phi(s) \tag{3}$$

where $\delta(t)$ is the Dirac delta function, α is the angle of attack and $\phi(s)$ is the indicial response. Once the response is found, the unsteady loads resulting from changes in angle of attack may be found through superposition of the responses, accomplished through a numerical solution of the convolution integral. Assuming the indicial response is known, the system output $y(t)$ is given by

$$y(t) = f(0)\phi(t) + \int_0^t \frac{df}{dt}\phi(t-\sigma)\,d\sigma \tag{4}$$

where $f(t)$ is the forcing function. For this problem, the forcing function is the angle of attack of the blade, Wagner's function is the indicial response, and the lift is the output. Although Wagner's function is known exactly for incompressible flow, its formulation is not convenient for an analytical solution. Instead, an exponential approximation, provided by Jones (Ref. 20), is used to simplify the problem.

$$\phi(s) \approx 1.0 - 0.165\,e^{-0.0455s} - 0.335\,e^{-0.3s} \tag{5}$$

The circulatory part of lift for a rigid airfoil starting from rest at $t=0$ inch response to a variation in angle of attack is given by

$$l^c(s) = \frac{1}{2}\rho V^2 S C_{l_\alpha}\left[\alpha(0)\phi(s) + \int_{s_o}^{s} \frac{d\alpha(\sigma)}{ds}\phi(s-\sigma)\,d\sigma\right] \tag{6}$$

Including noncirculatory (apparent mass terms), the total lift is given as

$$l(s) = C_{l_\alpha}\rho V^2 b\left[\alpha(0)\phi(s) + \int_{0}^{s} \frac{d\alpha(\sigma)}{ds}\phi(s-\sigma)\,d\sigma\right] + \pi\rho b^2(V\dot{\alpha} - ab\ddot{\alpha}) \tag{7}$$

per unit span, assuming V is constant, where a is the location of the pitch axis and b is the airfoil semi-chord (Ref. 21). For this case, the pitch axis is located at the quarter chord of the airfoil ($a=-\frac{1}{2}$). This equation is solved numerically for discrete values of time using a recurrence algorithm (Ref. 22).

Drag is calculated as the sum of the profile and induced components,

$$D = \frac{1}{2}\rho V^2 S\left(C_{D_o} + \frac{\left(C_{\mathrm{L}}^{\mathrm{c}}\right)^2}{\pi AR e}\right) \tag{8}$$

where C_{D_o} is the profile drag coefficient for the airfoil and $C_{\mathrm{L}}^{\mathrm{c}}$ is the circulatory component of the unsteady lift given by Eq. (6). Empirical data from Refs. 23 and 24 were used for the lift curve slopes as well as the profile drag coefficients, as these quantities have a strong dependence on Reynolds number. The data used for the present work are based on a NACA 0012 wing with an aspect ratio of six at a Reynolds number of 20,700. Note that the maximum Reynolds number of the present cycloidal rotor is approximately 17,000. The Oswald span efficiency factor is represented as e, and a value of $e=0.95$ was assumed as an initial guess. Although this method of determining drag is not typical, it provides an approach in which to directly incorporate empirical data relevant to the present work.

The moment of the airfoil about its pitching axis, may be derived in a similar manner as

$$M_{\mathrm{a}} = \pi\rho b^2\left[-Vb\left(\frac{1}{2}-a\right)\dot{\alpha} - b^2\left(\frac{1}{8}+a^2\right)\ddot{\alpha}\right] + C_{\mathrm{L}_\alpha}\rho V b^2\left(a+\frac{1}{2}\right)\left[\alpha(0)\phi(s) + \int_{s_o}^{s}\frac{d\alpha(\sigma)}{ds}\phi(s-\sigma)\,d\sigma\right] \tag{9}$$

Kinematics of the blade pitch mechanism

The above equations are dependent on α, $\dot{\alpha}$, and $\ddot{\alpha}$, which respectively represent the angle of attack, angular velocity, and angular acceleration of the blade about its pitch axis (quarter-chord). The variation of blade pitch angle as a function of azimuth can be derived by examining the kinematics of the blade pitch mechanism. The blade pitch angle can be idealized as a simple sinusoidal function, given by

$$\theta = -\theta_{\max}\sin(\Psi - \phi) \tag{10}$$

where ϕ is the angle of eccentricity of the offset link and Ψ is the position of the blade around the azimuth. The angle of attack may be found by subtracting the induced angle of attack, α_{dw}, from the blade pitch angle.

$$\alpha = \theta - \alpha_{dw} = -\theta_{\max}\sin(\Omega t - \phi) - \alpha_{dw} \tag{11}$$

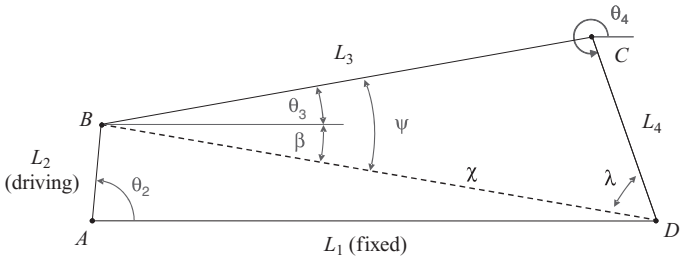

Fig. 12. Generic four bar linkage.

The angular velocity and acceleration, are the first and second derivatives of this function, respectively:

$$\dot{\theta} = -\theta_{\max}\Omega\cos(\Omega t - \phi) \tag{12}$$

$$\ddot{\theta} = \theta_{\max}\Omega^2\sin(\Omega t - \phi) \tag{13}$$

The pitch change mechanism does not produce a pure sinusoidal variation in blade pitch angle. This difference also affects the angular velocity and acceleration, which influence the noncirculatory components of lift. Therefore, it is necessary to calculate the exact kinematics of the pitch change mechanism to achieve accurate results. The mechanism in the experimental rotor utilizes a passive four bar mechanism to accomplish the blade pitch change. The various configurations of this type of linkage system may be found in a wide variety of mechanics or kinematics textbooks (Ref. 25). Figure 12 illustrates a generic four bar linkage. Let L_1, L_2, L_3, and L_4 denote the lengths of the four linkages, with L_1 being the fixed linkage. Angles θ_2, θ_3, and θ_4 give the angular positions of L_2, L_3, and L_4, respectively, and are measured counterclockwise from the horizontal plane. The diagonal, denoted by χ, runs from point B to point D. The angle from χ to L_3 is Ψ, while β is the angle from χ to L_1. L_2 is considered the driving linkage, and as such its angular position, θ_2, is known. Note that this is a simplifying assumption, as in the case of the experimental mechanism, L_2 is in the fixed frame of reference, and L_1, L_3, and L_4 are in the rotating frame. The procedure to obtain the kinematics of the mechanism involves examining the triangles *ABD* and *BCD* in all configurations of the mechanism, assigning vectors to each link and solving for the angles and rotational velocities of the links.

The angular velocity of link L_4, which is the blade, can be obtained as

$$\omega_4 = \frac{r_2\omega_2\sin(\theta_3 - \theta_2)}{r_4\sin(\theta_4 - \theta_3)} \tag{14}$$

Assuming the cycloidal rotor is not accelerating ($\alpha_2 = 0$), the angular acceleration is found as

$$\alpha_4 = \frac{r_3\omega_3^2 + r_2\omega_2^2\cos(\theta_2 - \theta_3) + r_4\omega_4^2\cos(\theta_4 - \theta_3)}{r_4\sin(\theta_3 - \theta_4)} \tag{15}$$

All angles, velocities, and accelerations are positive when measured counterclockwise. Thus, from the geometry of the linkage system, all the necessary terms may be determined as a function of θ_2. Figure 13 compares the actual blade pitch angle (θ_4), velocity (ω_4), and acceleration (α_4) of the mechanism used in the experimental rotor to an ideal motion in which the blade pitch angle varies sinusoidally with a magnitude of 25°. Note that there is a small difference between the blade pitch angle variation and a pure sinusoid. This difference is accentuated in the time derivatives of blade pitch angle.

In addition, the maximum pitch angles of the four bar linkage are not exactly ±25°. The linkage has a slightly larger pitch angle at $\Psi = 0°$ ($\theta = -26.11°$), and a slightly smaller one at $\Psi = 180°$ ($\theta = 24.07°$). This

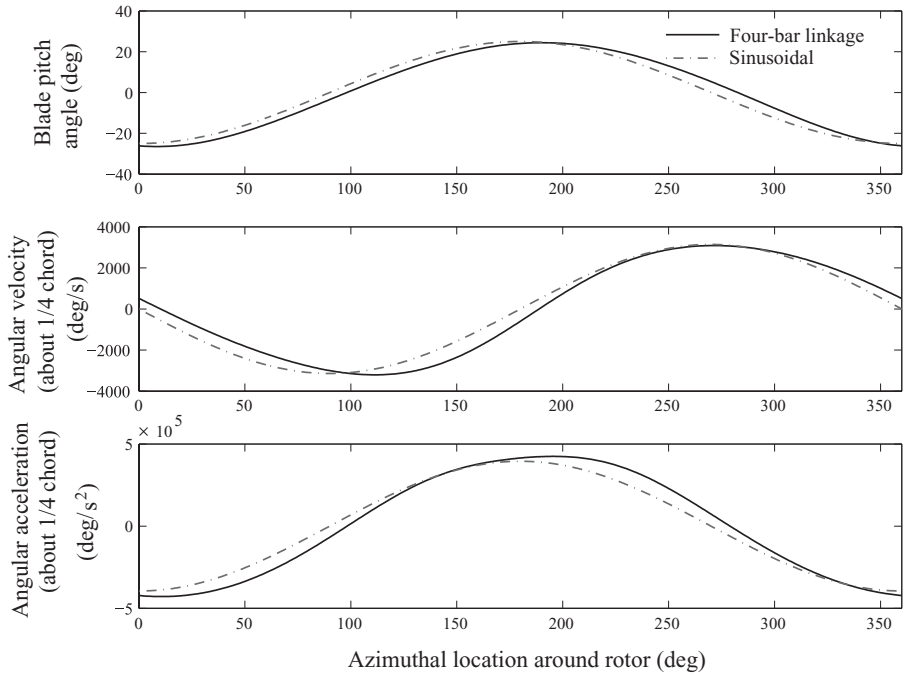

Fig. 13. Actual and ideal motion of blade pitch mechanism.

difference between the upper and lower pitch angle escalates as the maximum pitch angle increases, and is an inevitable product of using a four bar linkage. From Fig. 13, it can be seen that there is also a phase lag of approximately 10° between the sinusoidal and actual blade motions. The phase lag changes with the maximum blade pitch angle and is again a product of the four bar linkage.

Calculation of downwash

Once the blade positions are determined from the linkage kinematics, the induced angle of attack and effective angle of attack are calculated. The calculation of the downwash, and consequently, the induced angle of attack, is key to predicting the aerodynamic loads on the rotor. The interaction of each blade with its neighbors can be taken into account using cascade aerodynamics. This depends on the ratio of blade chord to blade spacing, which is commonly referred to as the "solidity" of the cascade, as well as on the Reynolds number (Refs. 26–28). Compressors typically have solidities of 1.0 to 1.5. The experimental cycloidal rotor in the six-bladed configuration has a solidity of 0.318. With only three blades, the solidity is half this value, or 0.159. At this value of solidity and at the Reynolds number of operation of the prototype cycloidal rotor, any cascade effects are expected to be weak, and are neglected in the present analysis.

The method of analysis employed to analyze the flow field around the cycloidal rotor is based on momentum theory, where the aerodynamic forces on the rotor are equated to the time rate of change of momentum through the rotor. This theory is based on the assumption that the induced velocity is constant along the blade chord and blade span. This method of analysis is similar to those used in the study of vertical axis wind turbines (VAWTs) (Ref. 29). Depending on the complexity of the problem and the accuracy necessary for the analysis, the models may further be classified into four types, shown in Fig. 14, where induced velocities are represented by u.

For the present analysis, an adaptation of double-multiple streamtube method was employed. In this model, the flow through the rotor is subdivided into a number of streamtubes, aerodynamically independent from one another and each with different induced velocities at the upstream and downstream halves of the volume swept by the rotor. Each streamtube intersects the rotor twice, once on the upstream side and again on the downstream side, as shown in Fig. 15. At each of the intersections, the rotor is represented by an infinitesimally thin actuator disk. Across each of these disks there is a pressure difference capable of generating axial momentum in the direction perpendicular to the disk. The induced flow passes through the actuator disks in a radial direction and is then deflected downward vertically. It is assumed that the steady value of downwash velocity is achieved within the rotor, and the wake velocity of the upper actuator disk is used as the free stream velocity for the lower disk (similar to a co-axial rotor system). Figure 15 illustrates the flow model used for the analysis. This flow model can be further simplified into an equivalent actuator disk model as shown in Fig. 16.

From basic momentum theory, expressions for the downwash velocities at each actuator disk can be derived as

$$w = 2v_{\mathrm{u}} \sin \Psi \tag{16}$$

$$v_{\mathrm{d}} = -\frac{1}{2} w \pm \sqrt{\frac{w^2}{4} - \frac{T}{2\rho d A} \cos \Psi} \tag{17}$$

where the thrust of the upper actuator disk is given by $T = \dot{m} w$. The induced velocities v_{u} and v_{d} are implemented in the program through an iterative scheme until convergence occurs. Note that an assumption is made in this flow model that the two actuator disks in each streamtube produce the same thrust. As such, it should be recognized that this is a tentative flow model, and has not been validated experimentally.

Rotor forces and moments

Lift and drag forces on each blade are first resolved into components normal and tangential to the cycloidal rotor motions:

$$F_{\tan} = L \sin \alpha + D \cos \alpha \tag{18}$$

$$F_{\mathrm{norm}} = L \cos \alpha - D \sin \alpha \tag{19}$$

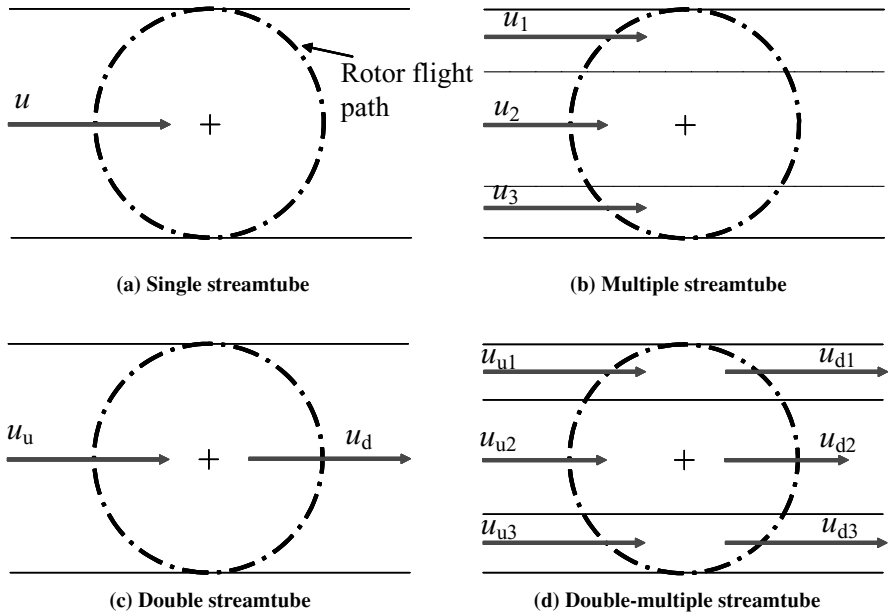

Fig. 14. Streamtube models.

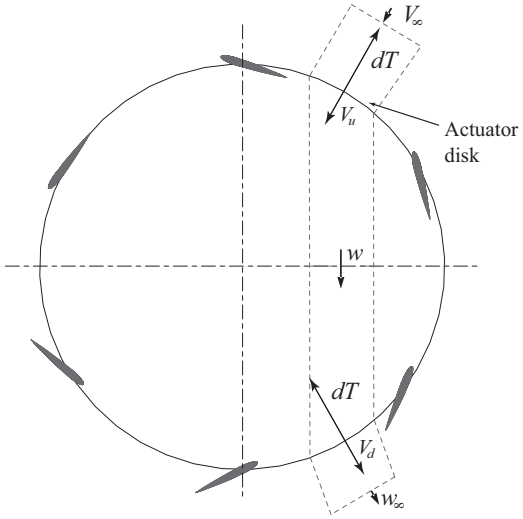

Fig. 15. Flow model used for hover analysis.

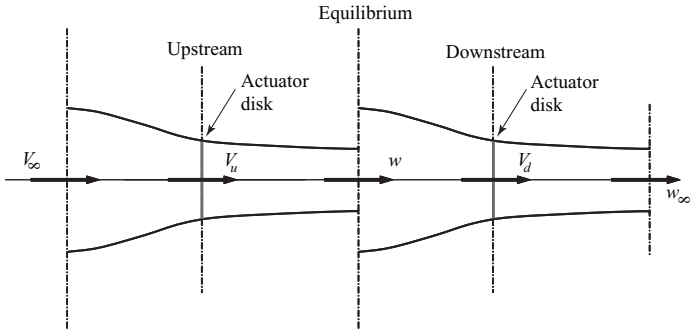

Fig. 16. Streamtube replaced by two tandem actuator disks.

where α is the angle of attack of each blade. The forces are now transformed into the x–z coordinate system (horizontal and vertical direction in relation to the cycloidal rotor). From Fig. 17, the transformation equations are found to be

$$F_x = F_{\text{norm}}\cos(\theta - 90) - F_{\tan}\sin(\theta - 90)$$
$$\Longrightarrow F_x = F_{\text{norm}}\sin\theta + F_{\tan}\cos\theta \tag{20}$$
$$F_z = F_{\text{norm}}\sin(\theta - 90) + F_{\tan}\cos(\theta - 90)$$
$$\Longrightarrow F_z = F_{\tan}\sin\theta - F_{\text{norm}}\cos\theta \tag{21}$$

By summing these total forces over an entire rotation, the average forces in the x and z directions may be determined. Total thrust produced by the cycloidal rotor per blade is given by

$$F_{\text{res}} = \sqrt{F_x^2 + F_z^2} \tag{22}$$

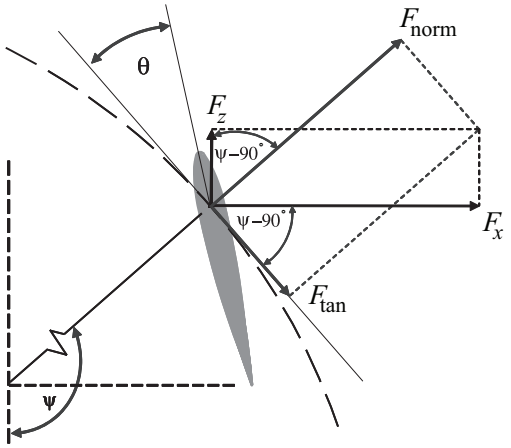

Fig. 17. Force components in x–z coordinate system.

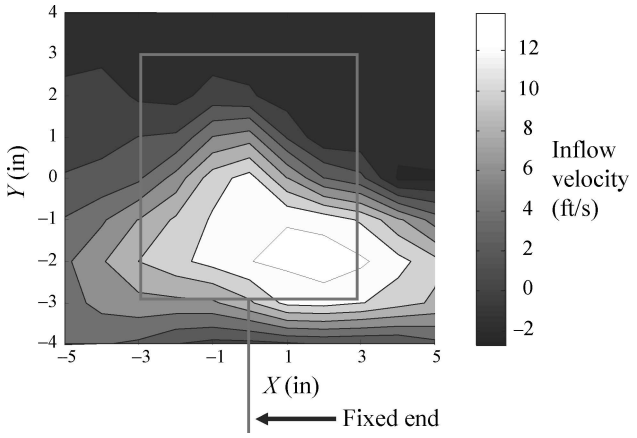

Fig. 18. Downwash distribution 3 inches below the cycloidal rotor axis at 1100 rpm, cantilevered condition.

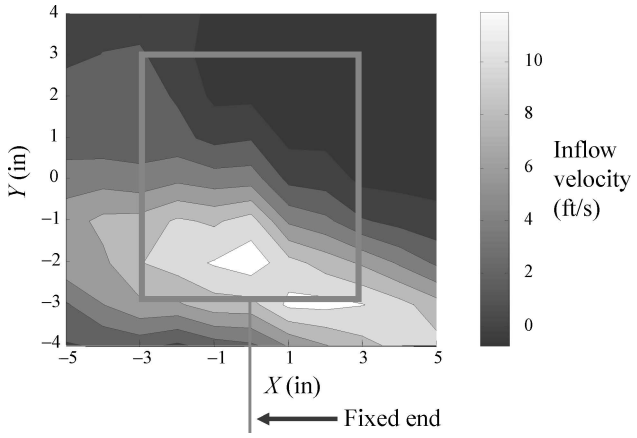

Fig. 19. Downwash distribution 9 inches below the cycloidal rotor axis at 1100 rpm, cantilevered condition.

The total torque about the rotor axis is given by

$$Q = \sum_{\text{Number of blades}} F_{\tan} R + \frac{M_{\text{tot}}\dot{\alpha}}{\Omega} \tag{23}$$

Power required by the rotor is obtained by

$$P = Q\Omega \tag{24}$$

Results and Discussion

Experiments were performed on the prototype cycloidal rotor to obtain a physical insight of the flow through the rotor as well as to obtain quantitative measurements of the performance of the rotor. As described above, the flow was visualized by means of pressure measurements and the loads were measured on an instrumented test rig. The pressure measurements were performed on a six-bladed rotor in cantilevered as well as clamped–clamped support conditions. The load measurements were carried out on a three-bladed and a six-bladed rotor, both in the clamped–clamped support condition.

Pressure measurements

Figure 18 illustrates the downwash at 3 inches (1/2 rotor diameter) below the cantilevered prototype rotor. The outline shows the position of the cycloidal rotor, rotating clockwise (toward the left side of the page). The downwash at 9 inches below the rotor is shown in Fig. 19. Note that the induced velocity distribution appears shifted toward the fixed end of the setup. This is undesirable as it is known that a nonuniform downwash distribution results in poor aerodynamic efficiency. It was surmised that vibrations in the rotor, in large part because of the flexibility of the cantilevered support, were the cause of this phenomenon.

The rotor was then tested with both ends clamped to investigate the effect of the support flexibility. Figure 20 illustrates the downwash distribution in the clamped condition. It can be seen that the flow is much more uniform than in the case of the cantilevered condition. This indicates that flexibility in the cantilevered support was the main cause of the nonuniformity in the downwash. The results of these pressure measurements is directly applicable to the implementation of the cycloidal rotor on a flight vehicle. While the cantilevered condition is the most attractive in terms of flight vehicle configuration, it should be kept in mind that the support should be as rigid as possible to obtain a favorable downwash distribution.

All subsequent data reported in this paper were obtained from the cycloidal rotor in the clamped–clamped condition. Figure 21 shows a

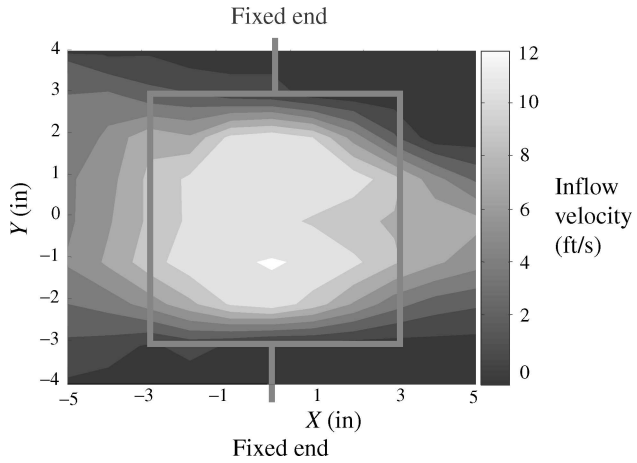

Fig. 20. Downwash 3 inches below cycloidal rotor, clamped condition at 1100 rpm.

cross-section of the flow measured at the mid-span of the rotor. The induced airflow through the top of the rotor is fairly uniform. Note that the inflow is greatest in the lower left quadrant of the rotor, and is swept in the direction of rotation to the right. Consequently, the resultant thrust vector of the cycloidal rotor is deflected slightly from the vertical.

Rotor thrust and power

The measured rotor thrust and power are expressed in terms of nondimensional parameters. The nondimensionalization is carried out with respect to a rotor reference area and the rotor blade tip velocity. For example, the rotor thrust coefficient is

$$C_T = \frac{T}{\rho(\pi b_r d)(\Omega R)^2} \tag{25}$$

where b_r and d are the length and diameter of the cycloidal rotor respectively, and T is the thrust (z-force). Note that $\pi b_r d$ is the swept area of the blades, and is equal to the total area of the actuator disks used in the derivation of the streamtube theory. The power coefficient is defined in a similar manner as

$$C_P = \frac{P}{\rho(\pi b_r d)(\Omega R)^3} \tag{26}$$

The vertical force is plotted against rotational speed in Fig. 22 for the six-bladed configuration, and in Fig. 23 for the three-bladed

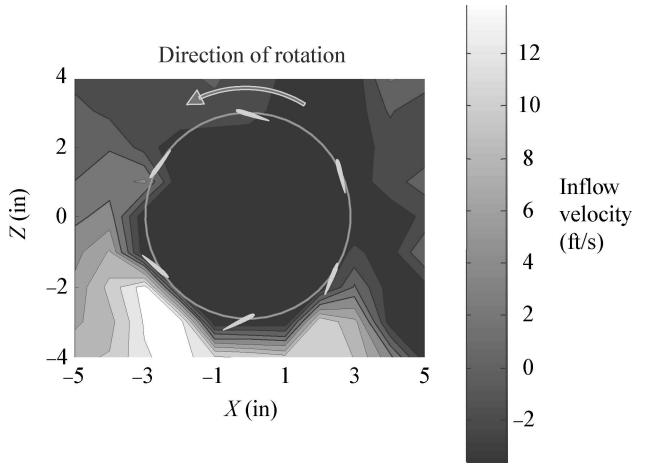

Fig. 21. Cross section of flow through cycloidal rotor at 1100 rpm.

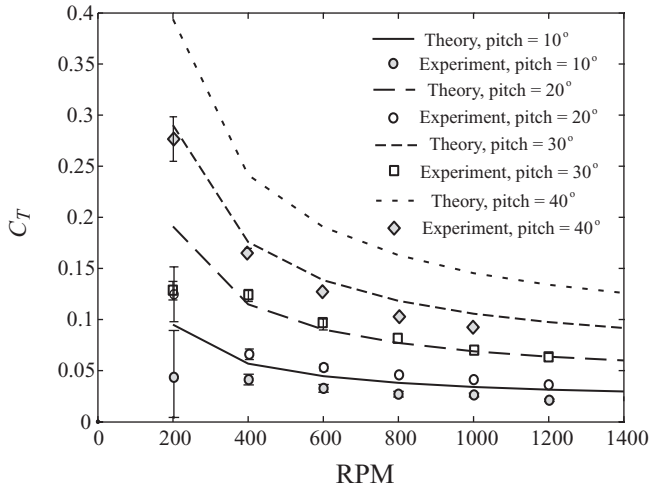

Fig. 22. Comparison of theory and experiment for a six-bladed rotor, z-force vs. rpm.

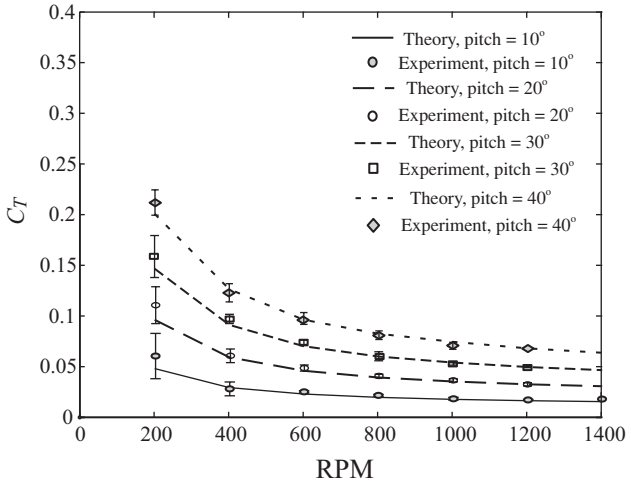

Fig. 23. Comparison of theory and experiment for a three-bladed rotor, z-force vs. rpm.

configuration. Theoretical predictions are also shown for both cases. Note that for the present rotor geometry, at a rotational speed of 1000 rpm, a coefficient of $C_T = 0.1$ corresponds to a thrust of approximately 0.57 N (58 g). It can be seen that the experimental data agree well with the predicted values for the three-bladed case. However, for the six-bladed configuration, the model significantly overpredicts the experimental results, especially for high pitch angles. This discrepancy may be due to flow interference between the blades in the six-bladed configuration. With six blades, there are approximately three chord lengths before the next blade hits the wake of the previous blade. The flow is still highly unsteady, and may have a profound effect on the impinging blade. It is probable that the assumption made in the analytical model that cascade effects between the blades are negligible may not be accurate.

An important detail to note is that the configuration with six blades does not produce twice the thrust of the three-bladed case. The blades on the downstream half of the rotor, from $\Psi = 270^\circ$ to 90°, see a significant downwash from the upstream blades. This results in an increase in induced velocity and a reduction in lift produced by the downstream blades. Thus, doubling the number of blades does not produce twice the lift. As blade pitch angle exceeds the static stall angle for the airfoil, there is no drop in thrust, with the implication that the rotor is not experiencing a stalled flow condition. This remains true even as the pitch angle reaches 30° and even 40°. There are two effects that may contribute to the unusually high pitch angle that the rotor can operate at without stall. First, the downwash through the rotor is significant, and this induced inflow would significantly decrease the effective blade angle of attack, particularly at $\Psi = 0^\circ$ and 180°, where pitch angle is the largest. Another possible contributing factor may be the occurrence unsteady aerodynamic phenomenon. This would result in a delay in flow separation to a higher angle of attack than typically seen in static stall, and as a result of this, the airfoil is able to achieve higher lift than would be possible in a static situation.

Pitch eccentricity

Referring to Figs. 4 and 12, the maximum blade pitch angles for the offset mechanism will occur when linkages L_2 and L_3 are parallel. However, the angle, θ_2, at which this takes place will vary depending on the desired maximum pitch angle. Therefore, to simplify data acquisition and maintain consistency in the measurements, the rotor was positioned such that L_2 was always vertical. Thus, from Fig. 24, the maximum blade pitch angles do not appear at $\Psi = 0$ and 180°, but at a phase lag approaching 10° with respect to direction of the offset. This results in a horizontal force produced by the rotor.

To determine the phase lag, or eccentricity, at which the maximum vertical thrust occurs, a series of experiments were conducted. Eccentricity is defined such that it is equal to zero when the offset for the pitch mechanism occurs at $\Psi = 180^\circ$. This is the position in which the thrust measurements shown in Figs. 22 and 23 were recorded. Note that at this condition, the rotor is thrusting toward the ground, eliminating any possibility of ground effect.

Figure 25 plots the experimental measurements as well as the predicted values for various eccentricity locations, for the six-bladed configuration. Note that if the eccentricity is shifted by 180°, the rotor thrust would be in the opposite direction with the same magnitude. It can be seen that the results agree very well with the predictions. As blade pitch angle is increased, the location of maximum thrust changes. From the model, for pitch angles of 0°, 10°, and 20°, maximum thrust occurs very close to an eccentricity of zero. However, at 30° pitch angle, maximum thrust occurs at an eccentricity of $+9^\circ$ (counterclockwise in Fig. 24), and at 40° it shifts to $+15^\circ$.

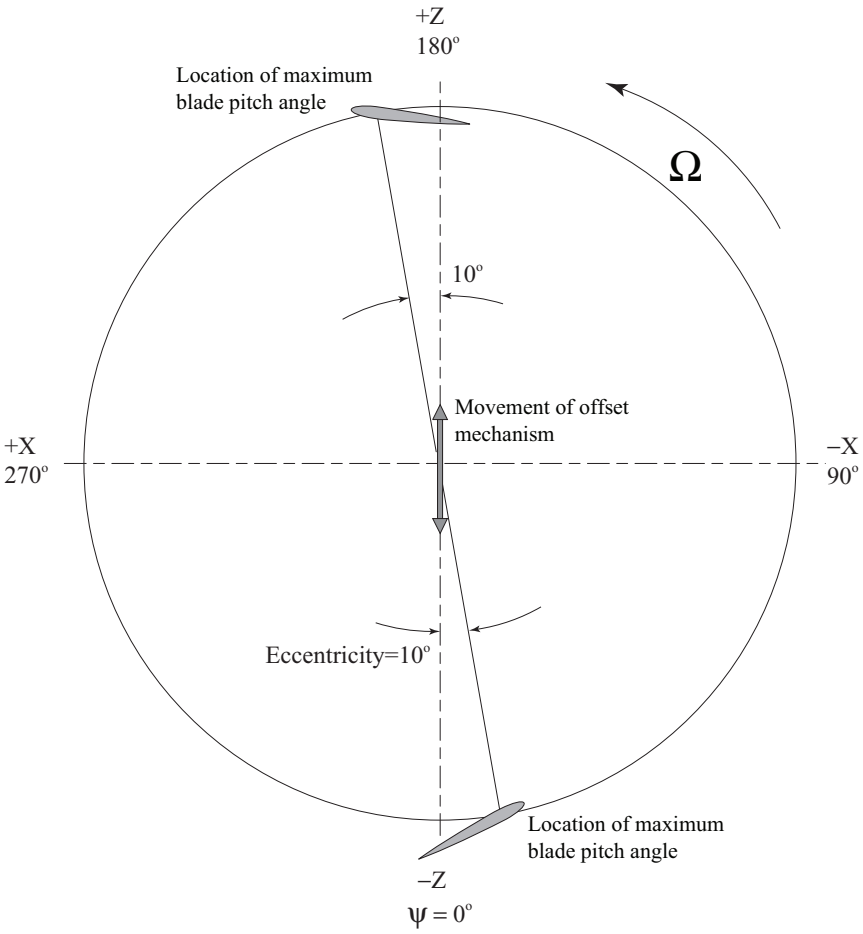

Fig. 24. Relationship between pitch angle and offset mechanism.

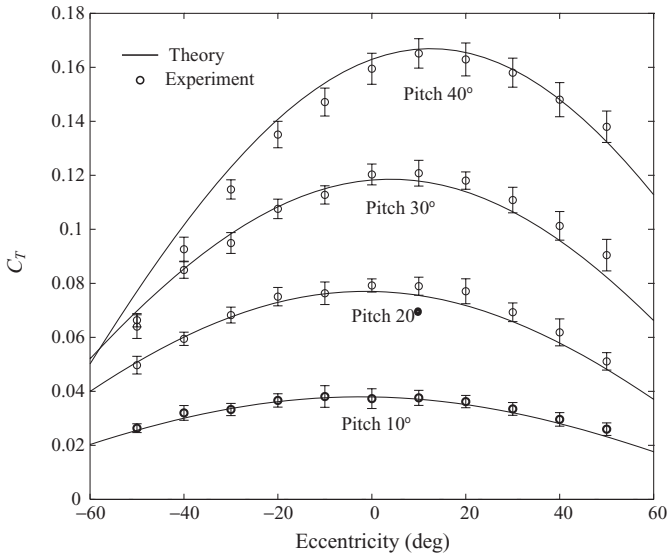

Fig. 25. Vertical force vs. offset eccentricity for six-bladed rotor.

Rotor power

The power consumed by the rotor is the summation of power required to overcome the aerodynamic forces as well as the power required to overcome mechanical friction and inertial forces in the mechanism. In order to assess the efficiency of the cycloidal rotor concept, and to compare it quantitatively with the efficiency of a conventional rotor, the aerodynamic power of both configurations must be compared. This can be obtained by performing a tare test on the cycloidal rotor. The tare test is performed by removing the blades from the cycloidal rotor and measuring the torque required to spin it over the entire range of rotational speeds. This gives a measure of the friction in the mechanism over the operational range of the rotor. The test is repeated for different settings of the offset mechanism, that translate to different values of maximum blade pitch. The measured mechanical power is then subtracted from the total power, yielding the aerodynamic power of the cycloidal rotor as a function of rotational speed for each blade pitch angle.

Figure 26 shows the total mechanical power consumed by the three-bladed cycloidal rotor, and Fig. 27 shows the aerodynamic power obtained after subtracting the frictional power measured from the tare tests. It can be seen that the total power is much larger than the aerodynamic power, especially at low blade pitch angles. This indicates an excessive amount of friction in the linkages of the four bar mechanism, as well as high drag on the rotating supports of the rotor blades. In addition, the frictional power shows a large increase at higher values of rotor speed. The design of the linkage mechanism for changing the pitch of the blades must be refined to minimize frictional losses and to successfully integrate the cycloidal rotor in a flight vehicle.

Figures 28 and 29 show the aerodynamic power consumed by the cycloidal rotor for the six-bladed and three-bladed cases. Predictions of power consumed are plotted for comparison. It can be seen that the experimental power consumed is higher than the predicted values at higher

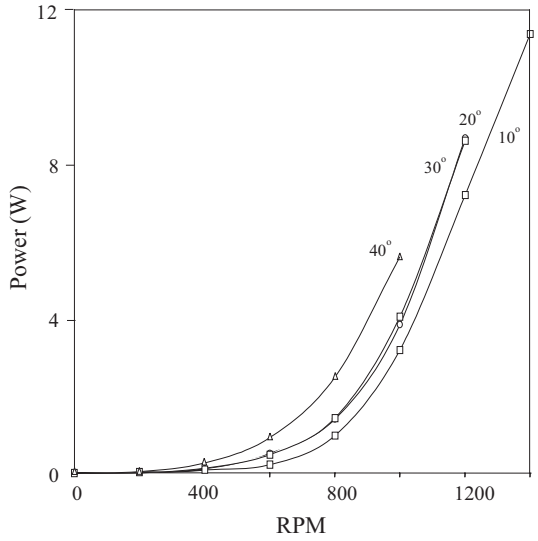

Fig. 26. Total power consumed by the three-bladed cycloidal rotor as a function of blade pitch angle.

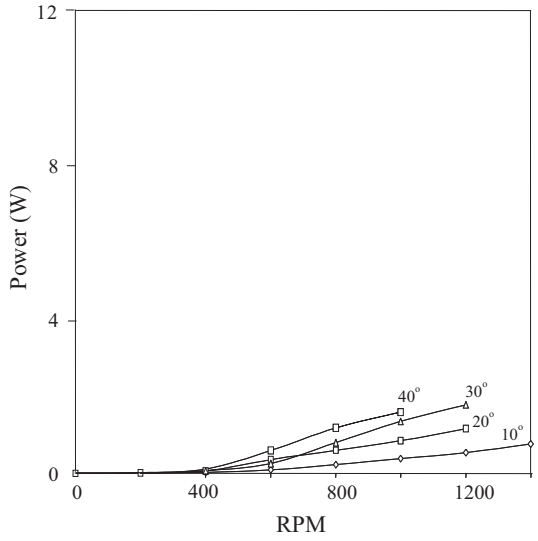

Fig. 27. Aerodynamic power consumed by the three-bladed cycloidal rotor as a function of blade pitch angle.

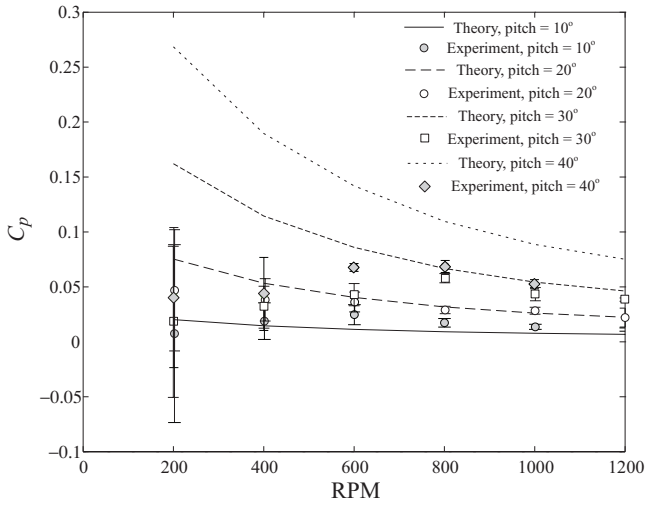

Fig. 28. Aerodynamic power consumed by the six-bladed cycloidal rotor as a function of blade pitch angle and rpm.

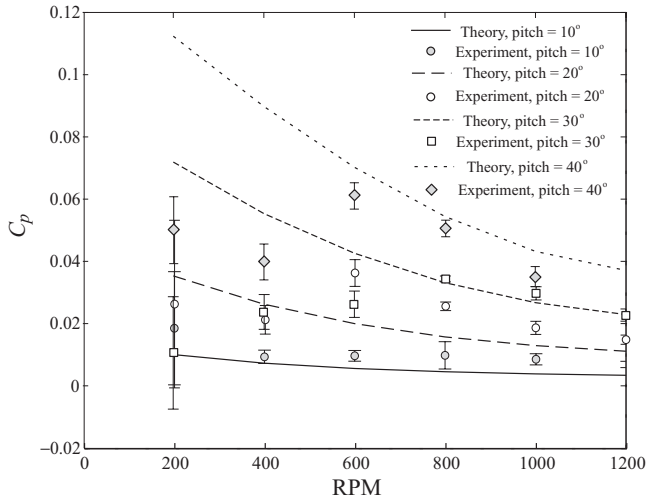

Fig. 29. Aerodynamic power consumed by the three-bladed cycloidal rotor as a function of blade pitch angle and rpm.

rotational speeds and is lower than predictions at lower rotational speeds. In general the power predictions do not agree with experimental results as well as the thrust predictions, however, the correlation is much better at higher rotational speeds. The errors may be due to incorrect constants such as C_{D_o} and e, as well as nonideal interaction between the blades, that is not captured by the analysis.

Comparison of the efficiency of the cycloidal rotor and a conventional rotor

To assess the potential of the cycloidal rotor concept, its hovering performance must be compared to that of a conventional rotor. A commonly used metric of hover performance is the rotor figure of merit. The ideal power consumed depends on the disk area of the rotor. For a conventional rotor, this area is clearly defined, however, for a cycloidal rotor, the disk area is somewhat ambiguous. For the nondimensionalization discussed above, the reference area was taken to be the swept area, which is the surface area of the cylinder described by the rotating blades. The disk area of the cycloidal rotor could also be considered as the rectangular area obtained by the projection of the rotor onto a horizontal plane. In addition, the figure of merit is typically plotted as a function of blade loading C_{T}/σ, which depends on rotor solidity σ, and is a measure of the mean lift coefficient C_{L} of the rotor blade. In the case of a cycloidal rotor, the rotor solidity is not clearly defined. One way to define solidity is based on the swept area of the rotor blades, yielding

$$\sigma_s = \frac{\text{blade area}}{\text{rotor area}} = \frac{N_{\mathrm{b}} c}{2\pi R} \tag{27}$$

where N_{b} is the number of blades, c is the blade chord, and R is the rotor radius. Based on this definition of reference area, the blade loading of the cycloidal rotor can be derived as

$$\frac{C_{\mathrm{T}}}{\sigma} = \frac{C_{\mathrm{L}}}{2} \quad \text{(swept area)} \tag{28}$$

Another way is to define solidity based on the projected area. However, as the projected area of each blade depends on its azimuthal location, a time averaged blade area, A_b can be defined as follows:

$$A_b = N_b b \frac{1}{\pi/2} \int_0^{\pi/2} c \cos\psi \, d\psi = \frac{2cbN_b}{\pi} \tag{29}$$

where $c \cos\psi$ is the projected chord of each blade at an azimuthal angle ψ. From this mean blade area, the solidity is

$$\sigma_p = \frac{N_b c}{\pi R} \tag{30}$$

Using this value of solidity and the projected area as the reference area,

$$\frac{C_T}{\sigma} = \frac{\pi C_L}{4} \quad \text{(projected area)} \tag{31}$$

Note that for a conventional rotor,

$$\frac{C_T}{\sigma} = \frac{C_L}{6} \tag{32}$$

It can be seen that the comparison of the cycloidal rotor and conventional rotor on the basis of figure of merit is dependent on the choice of an appropriate reference area. Therefore, a more physical metric is required as a basis for comparison.

From a practical viewpoint, the largest physical dimension is the most important constraint in the design of a micro aerial vehicle. As the rotor is typically sized to occupy as much as possible of the allowable vehicle dimension, a comparison of the performance of different lifting rotors can be made based on a constant rotor dimension. In the case of a conventional rotor, the critical rotor dimension is the rotor diameter, and in the case of a cycloidal rotor, it is the rotor span. For a given lifting rotor, the most important metric is the thrust produced for a unit input power (power loading). In addition, the absolute value of thrust produced is also important to be able to carry the maximum payload. Therefore, having a target weight and payload, the best rotor is the one with highest power loading at a given thrust, while fitting within a specified dimension.

To perform this comparison, the power loading of the cycloidal rotor was measured and compared to that of a conventional two-bladed rotor with a diameter equal to the span of the cycloidal rotor. The relevant parameters of the conventional rotor used in the comparison are provided in Table 2. Construction and testing of the rotor was performed by Hein and Chopra (Ref. 5). Testing was performed up to a blade tip Reynolds number of approximately 40,000.

The power loadings of the three-bladed and six-bladed cycloidal rotor are shown in Figs. 30 and 31, respectively. It can be seen that the six-bladed rotor has a higher power loading at a given value of thrust. In addition, the power loading is high at low values of thrust and decreases to an asymptote of about 25 g/W at high values of thrust. Both the three-bladed rotor and the six-bladed rotor asymptote to approximately the same value of power loading at high thrust levels. Figure 32 shows a comparison of the power loading of the conventional rotor and the six-bladed cycloidal rotor. Note that the power loading of the conventional rotor corresponds

Table 2. Parameters of the conventional rotor

Parameter	Value
Diameter	6 inches
Chord	0.787 inch
Airfoil camber	7%
Airfoil thickness	2.75%

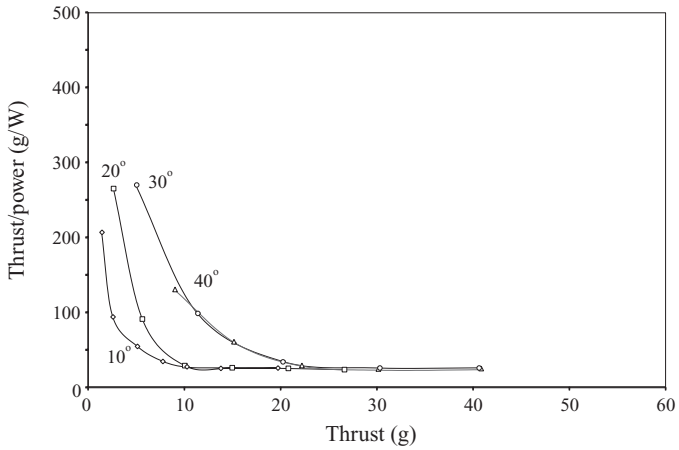

Fig. 30. Power loading of a three-bladed cycloidal rotor as a function of rotor thrust, for different blade pitch angles.

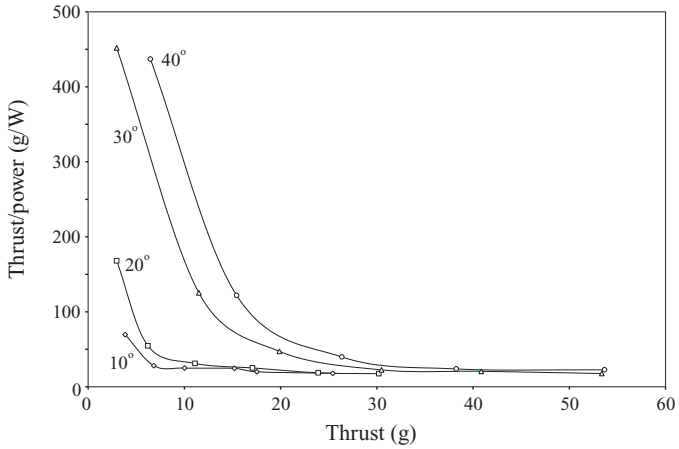

Fig. 31. Power loading of a six-bladed cycloidal rotor as a function of rotor thrust, for different blade pitch angles.

to an optimized rotor, with a best case figure of merit of around 0.55. The dashed lines represent curves of constant collective for the conventional rotor, and the shaded symbols represent the cycloidal rotor at different blade pitch angles. The power loading of the conventional rotor increases with increasing collective but is still less than that of the cycloidal rotor at blade pitch angles of 30° and 40°. It can also be seen that the conventional rotor can produce higher maximum thrust. However, the maximum rpm of the cycloidal rotor was limited in the test setup by mechanical considerations, which limited the maximum thrust produced.

Conceptual Design of a Cyclo-MAV

Based on the experimental results, a paper study was conducted to determine the feasibility of implementing the cycloidal propulsion concept on a micro air vehicle. A vehicle using two cycloidal rotors of the same dimensions as tested in the current work, was designed using CATIA. The complete vehicle design is pictured in Fig. 33.

Blades are to be constructed with a foam core covered by a carbon fiber skin, and with a carbon rod spar to stiffen the blade against the significant transverse centrifugal blade loading inherent in the cycloidal design. The blades will be attached at one end to a three-arm frame fabricated from carbon fiber; at the other end, the blades will be held together by a carbon

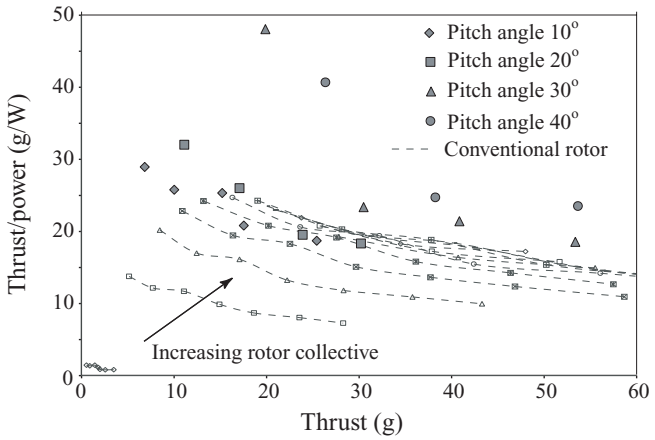

Fig. 32. Comparison of power loading of a cycloidal rotor and a conventional rotor.

ring. This design would eliminate a considerable amount of weight over the previous configuration, while still limiting the bending moment of the blade to acceptable levels.

Rotors will utilize a fixed pitch offset mechanism to achieve the required change in blade pitch angle (Fig. 34). Although a variable pitch mechanism was used on the experimental rotor, a fixed pitch design can be made much lighter. The mechanism will be set such that the maximum pitch angle of the blades is $\pm 30^{\circ}$.

Directional control of the vehicle will be achieved by rotating the driveshaft of each rotor, which will change the azimuthal location of the offset mechanism. The rotor driveshafts, both coincident with shaft bearings, will allow the rotors to rotate freely in any direction. The control mechanism will consist of two small servos, mounted between the rotors. Actuation of the servos, which will be connected to the driveshaft through a linkage arrangement, would rotate the entire rotor, changing the direction of thrust.

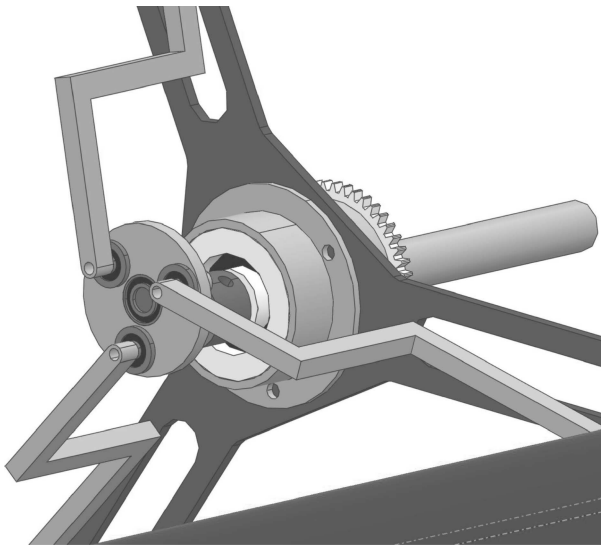

Fig. 34. Fixed pitch offset mechanism.

The electronics package and payload will be positioned below and aft of the rotor axes such that their weight, in conjunction with an appropriate fuselage attitude, would provide the necessary anti-torque to trim the vehicle. This setup would eliminate the need for an additional device for torque compensation and its accompanying weight penalty. A weight breakdown of the vehicle components is provided in Table 3, compared to the weight breakdown of a single rotor MAV (Ref. 1) of the same total weight. Note that the increased rotor weight of the cyclo-MAV is compensated for by a lower structure weight compared to the case of the single rotor MAV.

Based on the results from the paper study, the rotors on the cyclo-MAV will require a minimum rotational speed of 1650 rpm to achieve the necessary thrust of 125 g per rotor. A speed of 1875 rpm should provide enough additional thrust for propulsion and control. The main drawback

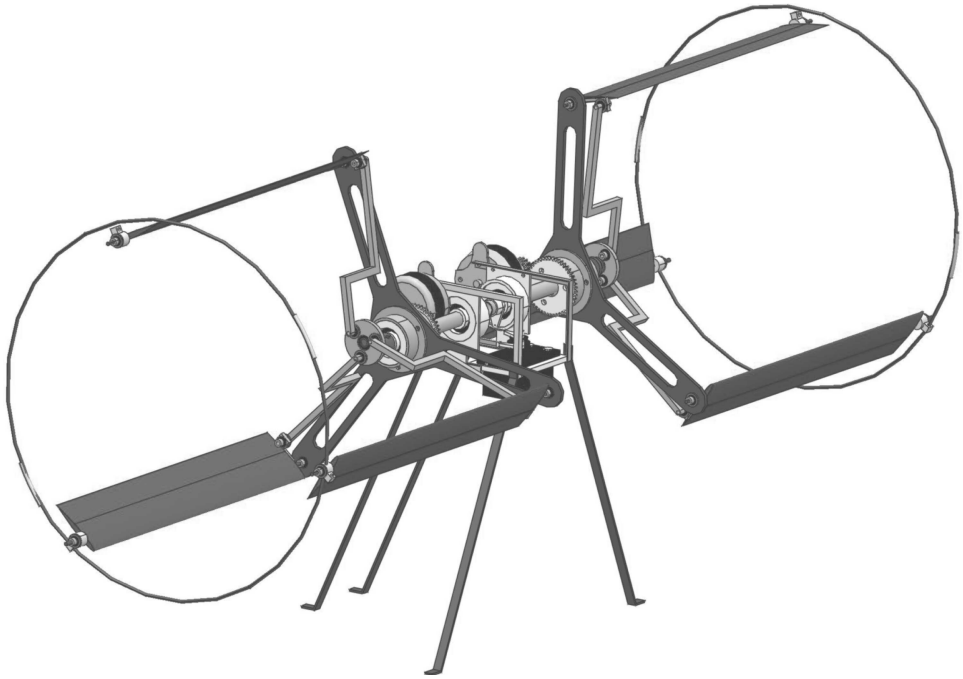

Fig. 33. Conceptual cycloidal rotor MAV.

Table 3. Component breakdown of cyclo-MAV compared with single rotor MAV (Ref. 1)

	Cyclo-MAV		Single Rotor MAV	
Component	Weight (g)	% Total	Weight (g)	% Total
Electronics and servos	38	15.3	38	15.9
Li-Po battery (700 mAh)	53.3	21.4	53.3	22.2
Motors	47.8	19.3	52.7	22
Rotor system	91.3	37.0	26.4	11
Structure	18.5	7.49	69.2	28.9
Total	248.9	100	239.6	100

of the cyclo-MAV is the complexity of the mechanical linkages, as well as the increased rotor mass. In addition, the present configuration is only suited for hover, and further research must be performed to investigate the forward flight characteristics of such a vehicle. The final evaluation between the cyclo-MAV and a conventional single or coaxial rotor MAV must involve all the aspects of the vehicle configuration, for example, the cyclo-MAV described above has a total span slightly more than that of two cycloidal rotors, while a conventional single or coaxial rotor MAV will have a total rotor diameter that will depend upon the size of tail rotor, and numerous other factors.

Conclusions and Future Work

A prototype cycloidal rotor of diameter 6 inches and span 6 inches was constructed and tested on a test rig capable of measuring thrust, torque and rotational speed. A theory was developed to predict the performance of the rotor, based on a streamtube momentum theory model in conjunction with a formulation of Wagner's function to account for unsteady aerodynamic effects. The main assumptions in the analysis were to neglect any influence of blades on each other, to consider equal thrust produced by the upper and lower halves of the rotor, and to assume uniform inflow on the rotor blades.

Thrust and power were determined as a function of rotational speed and blade pitch angle. Thrust increased with the square of rotational speed, while power increased with the cube of rpm. No dramatic reduction in thrust was measured as blade pitch angle was increased up to 40°, indicating that dynamic stall may play a role in the operation of the cycloidal blade system. Tests were conducted on both a six-bladed rotor and a three-bladed rotor. The six-bladed rotor was observed to produce only 30% more thrust than the three-bladed case at the same rpm and collective setting.

Predictions of the direction of the thrust vector as a function of eccentricity of the four bar linkage correlated well with measurements. Thrust predictions matched well with experiment for the three-bladed rotor, but were less accurate for the six-bladed rotor. This could be a result of interaction between the blades, which was neglected in the analysis. Tare tests revealed that a major component of the mechanical power consumed by the prototype cycloidal rotor was caused by friction, especially in the four bar linkage mechanism. Power predictions were satisfactory only at higher rotational speeds and were in general poor at lower speeds and high blade pitch angles. Compared to a conventional rotor of the same diameter, a higher power loading was observed, especially at low values of thrust. The power loading of both the three-bladed rotor and the six-bladed rotor decreased with increasing thrust and leveled off at approximately 25 g/W. Note that the power loading was calculated based only on the aerodynamic power of the cycloidal rotor.

An MAV utilizing cycloidal rotors was modeled and optimized for low weight. The complete vehicle, including electronics and battery, weighed approximately 250 g. Based on predictions, the rotors must rotate at 1650 rpm for the vehicle to produce sufficient thrust. From the present work, it appears that while the cycloidal blade system is a viable configuration for a micro air vehicle, the efficiency of the system is highly dependent on the mechanical design and on minimizing the friction in the linkages. The complexity and number of parts of the design are also subjects of consideration.

Future work involves optimization of the design to maximize its usefulness. Previous research has shown that the NACA 0012 is extremely sensitive to variations in Reynolds number or turbulence, and is unsuitable for Reynolds numbers less than 50,000. Blades with larger chords would increase Reynolds number and may prove beneficial, although any benefits may be offset by the increase in solidity of the rotor, which decreases performance. In addition airfoil profile better suited to low Reynolds number operation could be explored.

Computational fluid dynamics (CFD) analysis would not only be useful in validating existing experimental and theoretical results, but would provide a good means of understanding the flow conditions around the rotor. Although cascade aerodynamics does not appear to have a significant effect on the model, it was apparent from the data that some interactions between blades and blade wakes were taking place in the six-bladed configuration.

Finally, it must be remembered that the mechanism currently used to provide periodic changes in blade pitch is suitable only for hovering conditions. An investigation of the blade motions at various forward flight speeds, and the mechanisms needed for producing them, must be carried out. Individual blade control, while probably the optimal configuration, would be difficult to implement on a small vehicle and would incur a significant weight penalty. A series of cams, each optimized for different flight speeds may prove to be a workable solution. The efficiency and handling of a cycloidal rotor micro air vehicle must then be determined through systematic experiments.

Acknowledgments

This research was carried out under the Multidisciplinary University Research Initiative (MURI) grant W911NF0410176 from the Army Research Office with Dr. Tom Doligalski as Technical Monitor.

References

[1]Sirohi, J., Tishchenko, M., and Chopra, I., "Design and Testing of a Micro-Aerial Vehicle with a Single Rotor and Turning Vanes," American Helicopter Society 61st Annual Forum Proceedings, Grapevine, TX, June 1–3, 2005.

[2]Bohorquez, F., and Pines, D., "Hover Performance and Swashplate Design of a Coaxial Rotary Wing Micro Air Vehicle," American Helicopter Society 60th Annual Forum Proceedings, Baltimore, MD, June 7–10, 2004.

[3]Bohorquez, F., Samuel, P., Sirohi, J., Pines, D., Rudd, L., and Perel, R., "Design, Analysis and Hover Performance of a Rotary Wing Micro Air Vehicle," *Journal of the American Helicopter Society*, 48(2), April 2003, pp. 80–90.

[4]Bohorquez, F., and Pines, D., "Rotor and Airfoil Design for Efficient Rotary Wing Micro Air Vehicles," American Helicopter Society 61st Annual Forum Proceedings, Grapevine, TX, June 1–3, 2005.

[5]Hein, B., and Chopra, I., "Hover Performance of Micro Air Vehicles: Rotors at Low Re," American Helicopter Society International Specialists' Meeting on Unmanned Rotorcraft, Chandler, AZ, January 18–20, 2005.

[6]Prouty, R. W., *Helicopter Performance, Stability and Control*, Krieger Publishing Company, Malabar, FL, 1990.

[7]Kirsten, F. K., "Cycloidal Propulsion Applied to Aircraft," *Transactions of the American Society of Mechanical Engineers*, Vol. 50, (AER-50-12), 1928, pp. 25–47.

[8]Wheatley, J., "Simplified Aerodynamic Analysis of the Cyclogiro Rotating-Wing System," National Advisory Committee for Aeronautics, NACA-TN-467, 1930.

[9]Wheatley, J., and Windler, R., "Wind Tunnel Tests of a Cyclogiro Rotor," National Advisory Committee for Aeronautics, NACA-TN-528, 1935.

[10]Gibbens, R., "Improvements in Airship Control Using Vertical Axis Propellers," Paper No. AIAA-2003-6853, AIAA's Third Annual Aviation Technology, Integration, and Operations (ATIO) Forum, Denver, CO, November 17–19, 2003.

[11]Onda, M., Matsuuchi, K., Ohtsuka, N., and Kimura, Y., "Cycloidal Propeller and Its Application to Advanced LTA Vehicles," Paper No. AIAA-2003-6832, AIAA Third Annual Aviation Technology, Integration, and Operations (ATIO) Forum, Denver, CO, November 17–19, 2003.

[12]Gibbens, R. P., Boschma, J., and Sullivan, C., "Construction and Testing of a New Aircraft Cycloidal Propeller," Paper No. AIAA-1999-3906, 13th AIAA Lighter-Than-Air Systems Technology Conference, Norfolk, VA, June 28–July 1, 1999.

[13]McNabb, M., "Development of a Cycloidal Propulsion Computer Model and Comparison with Experiment," Master's Thesis, Mississippi State University, December 2001.

[14]Kim, S., Yun, C., Kim, D., Yoon, Y., and Park, I., "Design and Performance Tests of Cycloidal Propulsion Systems," Paper No. AIAA-2003-1786, 44th AIAA/ASME/ASCE/AHS Structures, Structural Dynamics, and Materials Conference, Norfolk, VA, April 7–10, 2003.

[15]Yun, C. Y., Park I., Lee, H. Y., Jung, J. S., Hwang, I. S., Kim S. J., and Jung, S. N., "A New VTOL UAV Cyclocopter with Cycloidal Blades System," American Helicopter Society 60th Annual Forum Proceedings, Baltimore, MD, June 7–10, 2004.

[16]Hwang, C. S., Hwang, I. S., Jeong, I. O., Kim, S. J., Lee, C. H., Lee, Y. H., and Min, S. Y., "Design and Testing of VTOL UAV Cyclocopter with 4 Rotors," Annual American Helicopter Society 62nd Annual Forum Proceedings, Phoenix, AZ, May 9–11, 2006.

[17]Paraschivoiu, I., Desy, P., and Masson, C., "Aerodynamics of Small-Scale Vertical-Axis Wind Turbines," Proceedings of the 20th Intersociety Energy Conversion Engineering Conference, Miami, FL, August 18, 1985.

[18]Paraschivoiu, I., Fraunie, P., and Beguier, C., "Streamtube Expansion Effects on the Darrieus Wind Turbine," *Journal of Propulsion and Power*, Vol. 1, 1985, pp. 150–155.

[19]Masson, C., "Dynamic and Viscous Effects on the Vertical-Axis Wind Turbine," Paper No. AIAA-1988-87, 26th AIAA Aerospace Sciences Meeting & Exhibit, Reno, NV, January 11–14, 1988.

[20]Leishman, J. G., *Principles of Helicopter Aerodynamics*, Cambridge University Press, New York, 2000.

[21]Bisplinghoff, R., Ashley, H., and Halfman, R., *Aeroelasticity*, Addison-Wesley Publishing Company, Cambridge, MA, 1955.

[22]Beddoes, T., "Practical Computation of Unsteady Lift," *Vertica*, Vol. 8, (1), 1984, pp. 55–71.

[23]Laitone, E., "Wind Tunnel Test of Wings at Reynolds Numbers Below 70,000," *Experiments in Fluids*, Vol. 23, 1997, pp. 405–409.

[24]Laitone, E., "Aerodynamic Lift at Reynolds Numbers Below 7×10^4," *AIAA Journal*, Vol. 34, (9), 1996, pp. 1941–1942.

[25]Harrisberger, L., *Mechanization of Motion*, John Wiley & Sons, New York, 1961.

[26]Gostelow, J. P., *Cascade Aerodynamics*, Pergamon Press, New York, 1984.

[27]Horlock, J., *Axial Flow Compressors: Fluid Mechanics and Thermodynamics*, Buttersworths Publications, Hertfordshire, UK, 1958.

[28]Johnsen, I., and Bullock, R. (editors), *Aerodynamic Design of Axial-Flow Compressors*, Paper No. NASA-SP-36, National Aeronautics and Space Administration, Washington, DC, 1965.

[29]Strickland, J. H., "A Review of Aerodynamic Analysis Methods for Vertical Axis Wind Turbine," Proceedings of the Fifth ASME Wind Energy Symposium, New Orleans, LA, February 23–26, 1986, pp. 7–17.